Coordinated spinal locomotor network dynamics emerge from cell-type-specific connectivity patterns

F David Wandler[1], Benjamin K Lemberger[1], David L McLean[2], and James M Murray*[1]

[1]Institute of Neuroscience, University of Oregon, USA
[2]Centre for Discovery Brain Sciences, University of Edinburgh, Scotland, UK

October 15, 2025

Even without detailed instruction from the brain, spinal locomotor circuitry generates coordinated behavior characterized by left-right alternation, segment-to-segment propagation, and variable-speed control. While existing models have emphasized the contributions of cellular- and network-level properties, the core mechanisms underlying rhythmogenesis remain incompletely understood. Further, neither family of models has fully accounted for recent experimental results in zebrafish and other organisms pointing to the importance of cell-type-specific intersegmental connectivity patterns and recruitment of speed-selective subpopulations of interneurons. Informed by these experimental findings and others, we developed a hierarchy of increasingly detailed models of the locomotor network. We find that coordinated locomotion emerges in an inhibition-dominated network in which connectivity is determined by intersegmental phase relationships among interneurons and variable-speed control is implemented by recruitment of speed-selective subpopulations. Further, while structured excitatory connections are not necessary for rhythmogenesis, they are useful for increasing peak locomotion frequency, albeit at the cost of smooth transitions at intermediate frequencies, suggesting a basic computational trade-off between speed and control. Together, this family of models shows that network-level interactions are sufficient to generate coordinated, variable-speed locomotion, providing new interpretations of intersegmental excitatory and inhibitory connectivity, as well as the basic, recruitment-based mechanism of speed control.

Introduction

It has long been known that the spinal cord is capable of generating locomotor movements even in the absence of detailed instructive input from the brain [1]. The core dynamical features of spinal locomotor circuitry are left-right alternation and rostro-caudal propagation of cyclical activity over a range of frequencies. These core features are most obvious during swimming in aquatic vertebrates [2], but they are also apparent during limbed locomotion [3, 4, 5, 6, 7, 8].

*jmurray9@uoregon.edu

Despite decades of work, the mechanisms by which rhythm is generated for coordinated locomotion are not yet fully understood. One line of research has focused on the intrinsic properties of individual excitatory spinal interneurons, whose mutual interactions serve to orchestrate rhythmic oscillations among downstream interneurons and motor neurons [9, 10, 11]. This perspective is supported by the observation of rhythmic bursting of excitatory interneurons in response to tonic input [12, 13], but it is potentially challenged by the observation that targeted disruptions of sources of phasic inhibition interfere with rhythmogenesis [14, 15, 16, 13]. Another line of work has suggested that rhythmic oscillations may be generated as a network-level phenomenon via random recurrent connectivity, without requiring specialized single-cell properties [17]. While this model is supported by the observation of "rotational" population dynamics rather than purely biphasic dynamics [17], the possible roles of particular cell types and their characteristic connectivity patterns are not addressed. In addition, the observation of recruitment of speed-selective interneuron populations [18, 11] and the functional roles of cell-type-specific intersegmental connectivity within spinal cord [19] have not yet been fully accounted for in either the cellular- or the network-level perspective.

Here, we construct a hierarchy of increasingly detailed models in which spinal central pattern generation occurs in a distributed manner, and the essential ingredients for producing coordinated locomotion are cell-type- and speed-specific connectivity motifs rather than specialized cellular properties or random connectivity. In all of these models, we represent individual neurons in a highly simplified way, so the dynamical properties of the network are entirely driven by emergent population dynamics due to connectivity patterns among units. First, we show that letting connectivity be determined by intersegmental phase relationships in a single-population, inhibition-dominated network is sufficient to account for left-right alternation and rostro-caudal propagation. Next, we show that dividing our units into fast- and slow-preferring populations is sufficient to account for variable-frequency control with constant phase lag via speed-dependent recruitment. Finally, in our most detailed model we show that the strength and modularity of recurrent excitation facilitates faster locomotion, but that there is a trade-off between maximum speed and controllability at intermediate speeds.

Together, these results point to an updated model of the spinal locomotor network as a distributed pattern generator, in which rhythm generation and other locomotion features emerge from collective population dynamics via patterned connectivity and speed-dependent recruitment.

Results

To investigate the degree to which population-specific connectivity patterns might account for the phenomenology of the spinal network described above, we developed a family of models at different levels of detail. In order to focus our investigation on connectivity patterns and the emergent population dynamics that result from them, we modeled the dynamics of individual neurons in a

highly simplified way:

$$\tau_i \frac{dr_i(t)}{dt} = -r_i(t) + \left[\sum_j W_{ij} r_j(t - \Delta_{ij}) + D_i \right]_+ , \tag{1}$$

where $r_i(t)$ is interpreted as the firing rate of unit i at time t, τ_i is the membrane time constant, D_i is the tonic drive, W_{ij} are recurrent weights from other units in the circuit, and $[.]_+$ denotes rectification. The axonal time delays Δ_{ij} are proportional to the number of segments between units i and j.

The three subsections that follow describe a hierarchy of increasingly detailed models, all of which are described by this basic dynamical equation. This approach enables us to focus mainly on basic computational properties within the relatively abstract, high-level model, whereas the lower-level models focus on implementation of distinct cell-type populations for obtaining additional features.

Phase relationships determine connectivity in a distributed pattern generator

Recent work mapping cell-type-specific connectivity patterns in zebrafish [20, 21, 19], mouse [22, 23], and other organisms has revealed a substantial presence of both excitatory and inhibitory connectivity traversing multiple segments. This is somewhat difficult to interpret in light of classical models of the spinal locomotor circuit, in which dynamical single-cell properties such as bursting or synaptic fatigue generate oscillations within each segment, and these oscillators are then coupled together with intersegmental interactions (see [24, 25, 26, 27] for reviews). We hypothesized that spatially patterned connectivity alone may be sufficient to drive coordinated locomotion even in the absence of dynamical single-cell properties. To test this, we constructed a high-level model in which dynamical single-cell properties are absent, and the basic features of left-right alternation and segment-to-segment propagation are driven by connectivity patterns. We took inspiration from "moving bump" models of brain circuits, for example in models of head-direction circuits, which have shown that inhibition-dominated, asymmetric connectivity can give rise to activation sequences [28, 29, 30]. Such models are also motivated by recent work in zebrafish demonstrating the importance of strong phasic inhibition for generating rhythmic locomotor activity [13]. This high-level model featured a single, homogeneous population of units described by Equation (1), where all units have identical membrane time constant τ and common excitatory input drive D.

The connections W_{ij} between units in this model were all set to be negative or zero, so that units in the model receive excitation only from the tonic drive, not from each other. Previous related work on threshold-linear recurrent networks with binary inhibitory weights and tonic input has shown that, despite their relative simplicity, such networks are capable of supporting rich dynamics [31]. Due to the (piecewise) linearity of the activation function, the magnitude of the nonzero weights has no effect on the dynamics, so we set $W_{ij} = -1$.

Given these simplifying choices, the nontrivial question in designing this model is which pairs of units should inhibit one another. The key principle that this model led us to is that the connectivity between pairs of units should encode the desired phase relationships between those units. A version

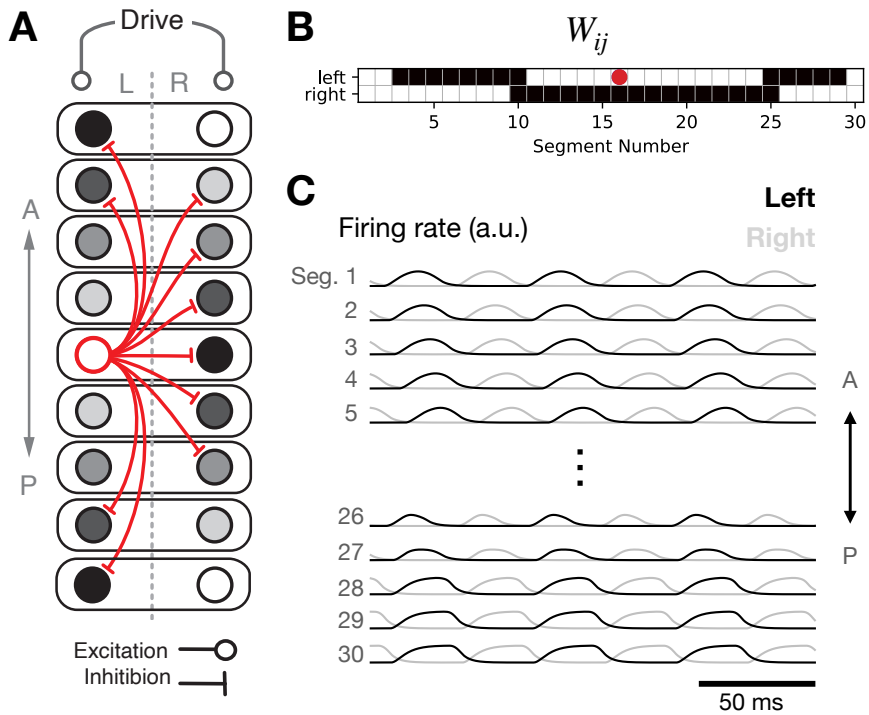

Figure 1: A single-population recurrent network generates rhythm, segment-to-segment propagation, and left-right alternation. **A**: Schematic connectivity diagram. Grayscale circles represent individual units at different phases of oscillation, with one unit per hemisegment. Red lines schematically illustrate inhibitory projections from a mid-body unit. **B**: Weight matrix illustrating all outgoing inhibitory projections from the mid-body unit labeled with a red dot. **C**: Time-dependence of network activity with all units receiving the same tonic drive. The different traces represent different units.

of this idea is already present in classical models, where left and right populations of neurons within each segment laterally inhibit one another, ensuring that they fire exactly out of phase. Here, we apply this same principle to model the longitudinal connectivity of the spinal locomotor network.

According to this principle, a mid-body unit should inhibit contralateral units in the same segment and in nearby segments, as well as inhibiting ipsilateral units more distally (shown schematically for a $N = 9$-segment model in Figure 1A). To make this precise, we can summarize the desired phase relationships for a pair of units i and j as follows:

$$\phi_{ij} = \frac{(s_i - s_j) \bmod N}{N} + \frac{(a_i - a_j) \bmod 2}{2}, \tag{2}$$

Where N is the number of segments. In this equation, s_i denotes the segment number of unit i, and $a_i = 0$ if unit i is in the left hemisegment or 1 if it is in the right hemisegment.

In order to realize these desired phase relationships, we set the connection strength from neuron

j to neuron i as $W_{ij} = f(\phi_{ij})$, where $\phi_{ij} \in [0, 1)$ is calculated from Equation (2), and

$$f(\phi) = \begin{cases} -1, & \phi_l < \phi < \phi_u, \\ 0, & \text{else.} \end{cases} \tag{3}$$

This equation describes local contralateral inhibition together with more-distal ipsilateral inhibition. Because $\phi_{ij} = 0.5$ for two units that are out of phase, it is necessary to choose $\phi_l < 0.5$ and $\phi_u > 0.5$. Further, in order for propagation to proceed head-to-tail rather than tail-to-head, it is necessary for the connectivity to be asymmetric, with a relatively larger window of disinhibition downstream and a relatively smaller window of disinhibition upstream. Hence, we chose $\phi_l = 0.3$ and $\phi_u = 0.8$ to define the window of inhibition. Finally, we can note that the most-distal ipsilateral projections described by Equation (3) (of length $\gtrsim N/2$) are not actually necessary, since the units targeted by such inhibition already receive contralateral inhibition from nearby active units on the opposite side. Indeed, such long-range projections are not typically found in the zebrafish [32, 33, 34]. Hence, in this model and in the others presented below, all connections between segments more than 13 segments apart were set to 0 (Figure 1B).

Driving this network with tonic input, and setting the axonal delay $\Delta_{ij} = 0$ for simplicity, we observed the key features of coordinated locomotion: phasic bumps of activity in each segment, with smooth propagation of the bump from head to tail and strict alternation between left and right within each segment (Figure 1C). While this high-level model is a highly simplified and abstract representation of the spinal locomotor network, it illustrates several key ideas that may be relevant for characterizing locomotor circuitry in biological organisms and will continue to be present in the more elaborate models developed in the following subsections. First, rhythm can be generated by the network as a whole, rather than by dynamical single-neuron properties or single-segment oscillations. Second, the network's recurrent connectivity is dominated by inhibition, illustrating that inhibition is capable of and perhaps necessary for sculpting the dynamics. Finally, the pattern of inhibitory connectivity is determined by the desired phase relationships between pairs of units. In the following sections, we will build upon this model by introducing multiple interneuron populations and allowing for more-heterogeneous connectivity between units.

Fast and slow speed modules implement frequency control via recruitment

While the single-population model described above was able to implement coordinated locomotion, it did so at a single, fixed frequency. This frequency was set by the only timescale in the model: the membrane time constant. Inspired by observations of *speed-module* structure in spinal circuitry in zebrafish [35] and mouse [36], whereby interneurons are recruited at either fast or slow locomotion speeds but not both, we made a minimal change to our initial model that introduces an additional timescale, replacing each unit by two units: a "fast" unit with a 1-ms membrane time constant, and a "slow" unit with a 10-ms time constant, as observed experimentally in larval zebrafish [37]. Trivially, in the absence of connectivity between the fast and slow modules, this model amounts to two copies of our earlier model and is capable of operating at two speeds: a fast speed if tonic

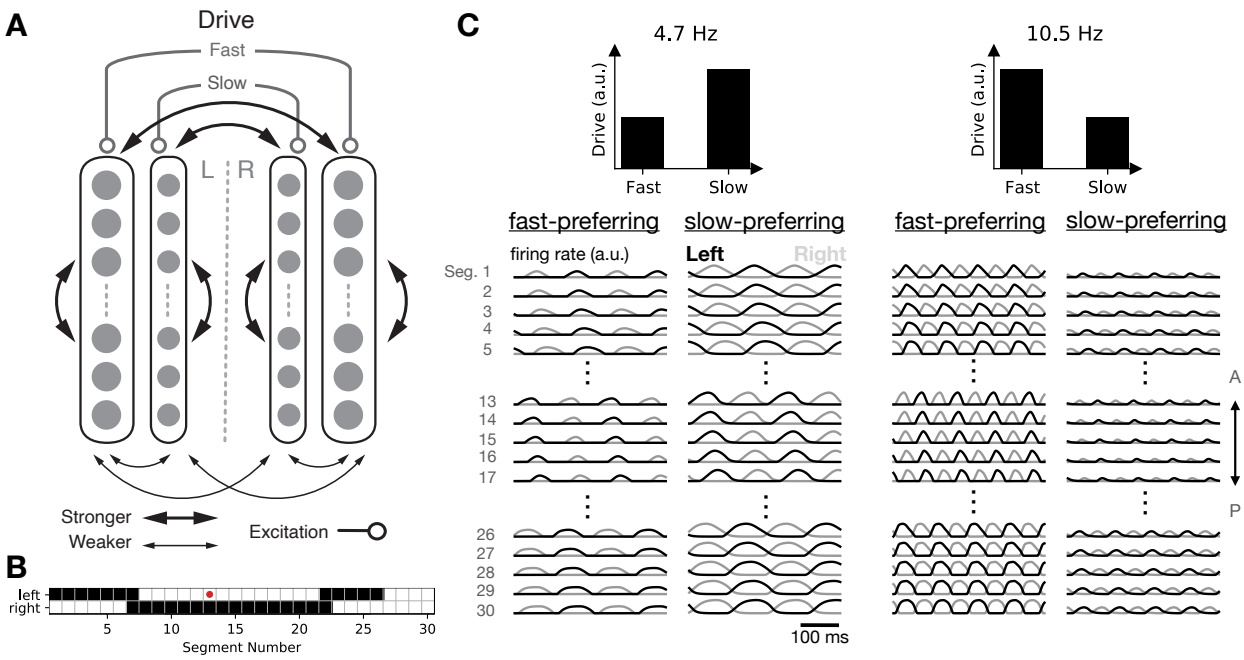

Figure 2: Fast and slow speed modules enable control of locomotion frequency. **A**: Connectivity schematic illustrating that fast- and slow-module units receive distinct tonic drives and project both within and between modules. **B**: Map of outgoing projections from a mid-body unit (red). **C**: Time-dependent activity of fast- and slow-module units given different levels of tonic drive to the two populations.

input is provided only to the fast-preferring units, and a slow speed if tonic input is provided only to the slow-preferring units [38]. In each case, the period of left-right alternation and head-to-tail propagation would be roughly proportional to the corresponding membrane time constant (though perhaps not perfectly proportional if axonal delays are included).

In order for the two parts of the network to oscillate at a single global frequency and to interpolate continuously between slow and fast speeds, connectivity between the two modules is required. To begin, we adopted the simplest choice and made the connectivity weights the same for between-module projections and within-module projections, with the same spatial connectivity patterns for between- and within-module projections (Figure 2A-B). We found that the circuit exhibited coordinated locomotion characterized by head-to-tail propagation and left-right alternation at a single global frequency that was intermediate between the characteristic frequencies of the fast and slow modules. Further, the locomotion frequency could be controlled in a graded manner by driving the two modules with different inputs. Locomotion was fast when the fast units received most of the tonic drive, and it was slow when the slow units received most of the tonic drive, with smooth interpolation of intermediate frequencies as the ratio of tonic drives was varied (Figure 2C).

Analyzing the model in greater detail revealed that varying the relative levels of tonic drive to the two populations strongly modulated the frequency (Figure 3A,B). This is made possible by selective recruitment of fast and slow speed modules, such that the fast population is active at faster

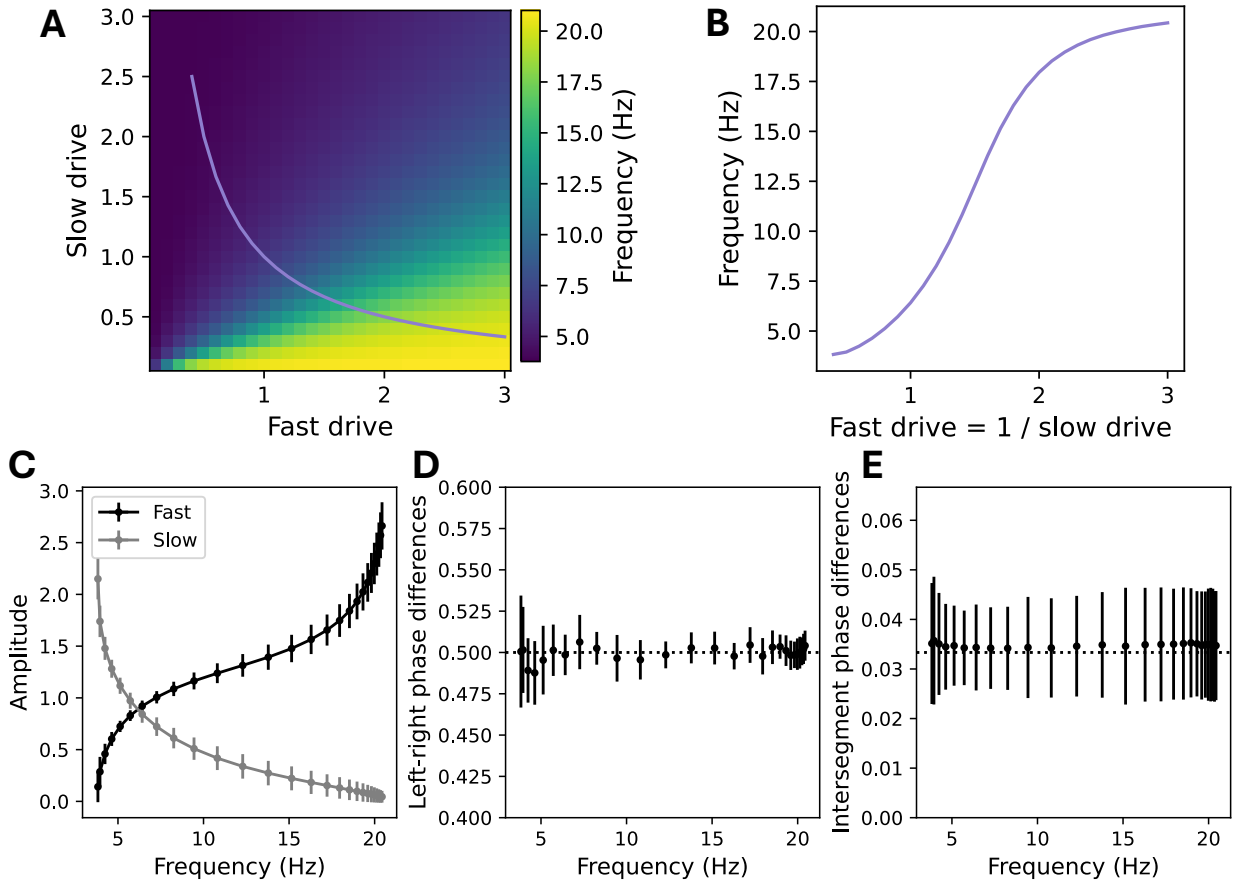

Figure 3: Speed-module recruitment enables frequency and amplitude control. **A**: Locomotion frequency with different levels of tonic drive to fast and slow units. **B**: Average amplitude and frequency along the path shown in (A). **C**: Frequency-dependent recruitment of fast and slow units as a function of locomotion frequency along the path shown in (A). **D**: Phase difference between left and right units within each segment (dotted line corresponds to half of a period). **E**: Phase difference (where 1 corresponds to a full period of oscillation) between pairs of units on the same side in adjacent segments (dotted line corresponds to $1/N$, where $N = 30$ is the number of segments). Error bars in all panels denote standard deviation across units.

locomotion frequencies, while the slow population is active at slower locomotion frequencies, with a smooth crossover between these two regimes (Figure 3C). Such recruitment has been observed experimentally [35] but has not been accounted for by previous models. In Figure S1, we further show that the disengagement of the slow module as frequency increases can occur due to inhibition from the increasingly active fast module, without requiring changes in the tonic drive to the slow population, which is also observed experimentally [35].

To establish that the model exhibits coordinated locomotion across all frequencies, we additionally computed the left-right phase difference between the pairs of units on either side of each segment, finding that the phase differed by half of a period across all locomotion frequencies (Figure 3D). We then computed the phase difference between pairs of units in adjacent segments, finding that this phase was approximately equal to $1/N$ across all locomotion frequencies, where N is the number of segments (Figure 3E), so that the length of the spinal cord exhibits approximately one period of oscillation. This *constant phase lag* relationship is a core feature of locomotion that has been observed during swimming in a variety of animals [39]. While it does not appear by default in models that chain individually oscillating segments together via longitudinal excitation, constant phase lag emerges in our model as a natural consequence of the fact that the desired phase relationships between segments are built into the circuitry via long-range inhibitory projections. Because the phase relationships are determined by the connectivity, which is the same at all speeds, the phase relationships do not depend on locomotion frequency.

These results show that, by including fast and slow subpopulations and coupling these subnetworks together, the model succeeds in producing coordinated locomotion across a broad range of frequencies, with control of frequency via selective recruitment of the two subpopulations. While this model succeeds in producing much of the phenomenology of the spinal locomotor network, it does not yet fully address the diversity of excitatory and inhibitory cell types that are known to play a role in the biological circuitry [19]. We turn our attention to this question in the following section.

Excitatory and inhibitory cell types

To address the role of cell-type-specific connectivity patterns in greater detail, we next incorporated excitatory and distinct inhibitory populations by replacing each unit in the above model with four units, leading to an eight-population model (since each of the four types has fast and slow subtypes) (Figure 4A). One of these populations (corresponding to V2a interneurons in the zebrafish) consisted of excitatory units with descending, ipsilateral projections. The other three populations consisted of inhibitory units, essentially breaking the inhibitory population from the earlier model into three populations that have identical activity (since they all receive the same inputs) but differ in their projection targets. One population of inhibitory units (corresponding to V1 interneurons in the zebrafish) had ascending, ipsilateral projections; another (corresponding to V2b interneurons in the zebrafish) had descending, ipsilateral projections; and a third (corresponding to dI6 and V0d interneurons in the zebrafish) had contralateral projections. The tonic drive was provided equally

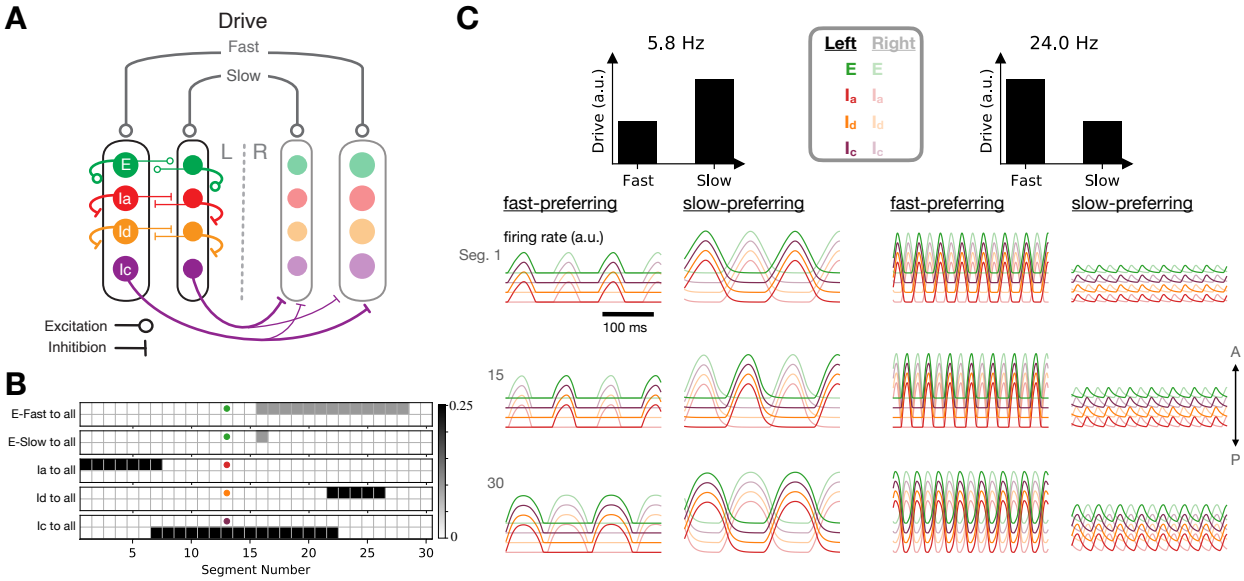

Figure 4: A model with excitatory and inhibitory populations. **A**: Schematic diagram illustrating connectivity among cell types (but not longitudinal connectivity) for the eight-population model. **B**: Detailed connectivity matrices for an example mid-body unit from each population. **C**: Time-dependent activity traces at slow (left) and fast (right) locomotion frequencies (traces are slightly offset for clarity).

to all units.

The outgoing spatial connectivity of each of these cell types is illustrated in Figure 4B. Each cell type projects equally to all of the units within each segment that it targets, so that all units within each segment receive the same inputs. As in the two-population model above, we set the spatial connectivity patterns for the inhibitory units according to the desired phase relationships between units, with short-range contralateral inhibition and intermediate-range ipsilateral inhibition. For the excitatory units, we assumed that the projections are descending only in order to facilitate head-to-tail propagation. All units within each speed module had the same membrane time constant and axonal conduction velocity.

Before analyzing the full model in detail, we decoupled the two speed modules from one another and began by studying the effects of various single-cell and cell-type-specific connectivity properties on the characteristic oscillation frequency of an individual speed module. Unsurprisingly, the locomotion frequency depended strongly on the membrane time constants, with smaller values of these parameters leading to faster frequencies (Figure 5A-B). Because the characteristic frequencies of the two speed modules set the upper and lower limits of locomotion frequency once the modules are coupled together in the full model, it is likely advantageous for an organism to have values of these parameters that differ strongly in fast- and slow-preferring neurons. This agrees with observations from the zebrafish, where the membrane time constants and axonal delays differ for fast- and slow-preferring excitatory and inhibitory interneurons [40, 37]. For our subsequent simulations, we fixed

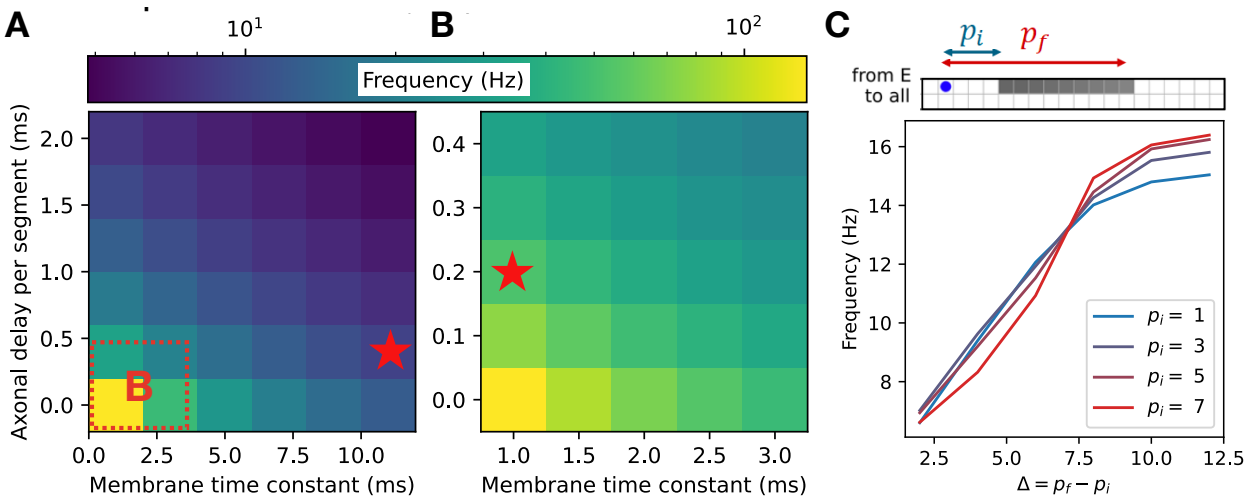

Figure 5: Single-cell properties and excitatory connectivity influence locomotor frequency in an individual speed module. **A, B**: Dependence of locomotion frequency on the axonal delay per segment and membrane time constant of units ((A) shows a broad range of values; (B) shows an inset from (A)). Stars denote experimentally observed values for fast and slow excitatory V2a cells in zebrafish [40, 37] **C**: Dependence of locomotion frequency on the projection distances of excitatory connections originating from the excitatory unit labeled blue.

these parameters for the fast and slow modules at the experimentally determined values indicated in Figure 5A-B [40, 37].

We next investigated the effect of connectivity properties on locomotion frequency for the decoupled speed module. We found that the frequency was modulated by more than a factor of two as the excitatory projection distances were varied (Figure 5C). This agrees with observations from zebrafish, where the extents of intersegmental projections have been shown to differ for fast- and slow-preferring excitatory interneurons, with fast-preferring V2a interneurons projecting more distally than slow-preferring V2a neurons [20]. For our subsequent simulations, we fixed these parameters for the fast and slow modules at the experimentally determined values illustrated in Figure 4B [20].

Having shown that the spatial extent of excitatory projections has a strong effect on locomotion frequency, we next asked whether varying connectivity properties would also modulate the range of possible frequencies in the full model with two coupled speed modules. Varying the global strength of excitatory projections had a strong effect on the range of possible frequencies, with stronger excitation facilitating faster locomotion (Figure 6A). In particular, whereas the purely inhibitory model with experimentally determined membrane time constants and axonal conduction velocities realizes a maximum frequency much lower than that observed in larval zebrafish (approximately 20 Hz, black line in Figure 6A), the inclusion of excitatory interneurons facilitates maximum frequencies of over 50 Hz, which is approaching peak swim speeds in larval zebrafish [13]. Thus, while excitatory interneurons are not necessary for producing coordinated locomotion in our model, they

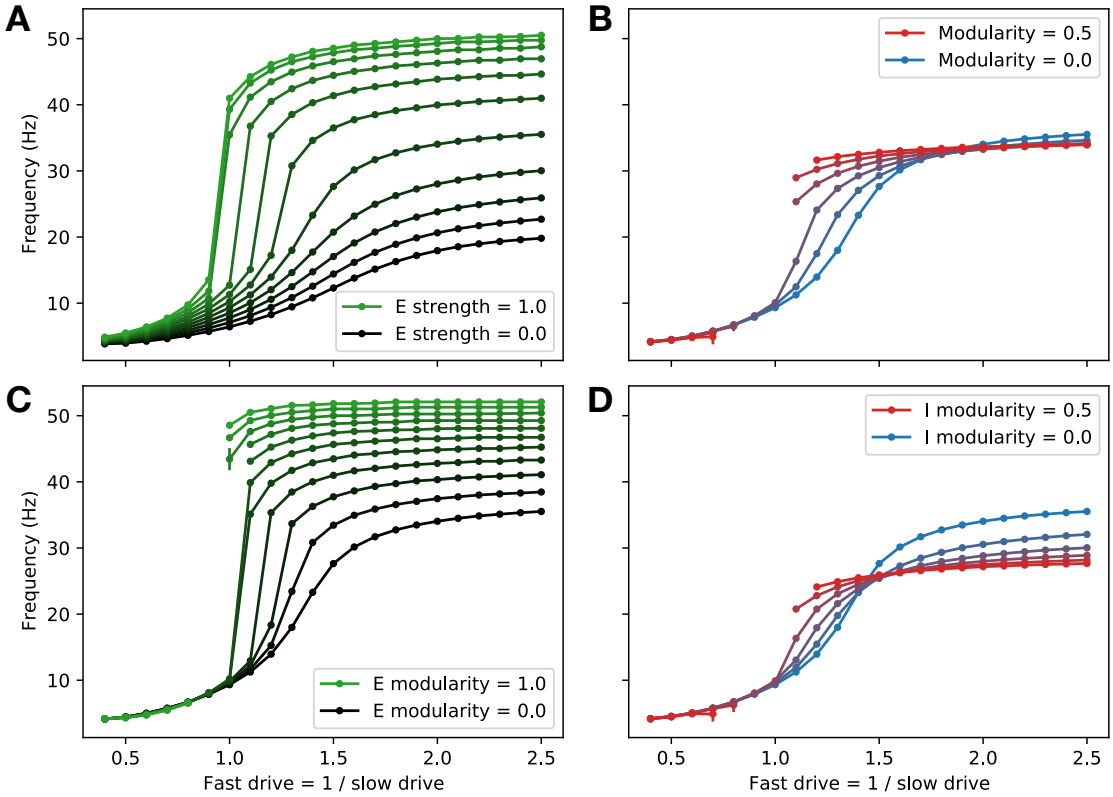

Figure 6: Frequency range depends on excitatory projection strength and modularity **A**: Dependence of the range of possible locomotion frequencies on the global strength of excitatory projections relative to that of inhibitory projections. **B**: Dependence of the frequency range on connectivity modularity, which quantifies the strength of inter-module (fast-to-slow and slow-to-fast) projections relative to intra-module (fast-to-fast and slow-to-slow) projections. (Missing intermediate points correspond to cases where coordinated locomotion does not appear.) **C**: Dependence of the frequency range on connectivity modularity of excitatory units, where inhibitory units have modularity set to zero. **D**: Dependence of the frequency range on connectivity modularity of inhibitory units, where excitatory units have modularity set to zero. (In (A), modularity is set to zero; in (B)-(D), strength of excitation is set to 0.4.)

do facilitate faster locomotion, suggesting that this may be a fundamental role for feedforward excitation in the spinal network.

Given that connectivity within and between speed modules has been shown in zebrafish to be modular, with stronger projections within modules than between modules [12], we asked what would be the effect of varying modularity in the model. We defined modularity as the difference between intra- vs. inter-module connection strength divided by the sum of these quantities, such that modularity of 1 corresponds to fully decoupled modules, while modularity of 0 corresponds to identical connection strengths within *vs.* between modules.

Varying the modularity of all four populations together, we found that there was essentially no effect on the maximum or minimum possible frequencies. Further, the model lost the ability to produce locomotion at intermediate frequencies as modularity was increased (Figure 6B). However, when we varied modularity among only the excitatory or only the inhibitory populations, we observed much more significant changes in the maximum frequency (Figure 6C-D). These changes occurred in opposite directions, with excitatory (inhibitory) modularity favoring faster (slower) speeds, suggesting that the lack of an observed change in frequency range when both types of modularity were varied together (Figure 6B) was due to cancellation between these two effects.

Together, these results show that the strength of feedforward excitation and the modularity of excitatory connectivity have a strong effect on the range of possible locomotion frequencies. There is a trade-off, however, in that the model loses the ability to smoothly interpolate between fast and slow frequencies in cases where the excitatory connectivity becomes too strong or too modular (Figure 6A,C). This requirement that excitation not be too strong is in accord with experimental observations from zebrafish [13], which have shown that peak excitatory post-synaptic currents are much weaker than peak inhibitory post-synaptic currents in V2a interneurons, consistent with the possibility that excitation may be globally weaker than inhibition in the spinal circuitry. Further, the fact that the model exhibits a frequency range similar to that of the zebrafish for parameters that are close to the critical values where smooth frequency control becomes impossible suggests that the spinal locomotor circuit faces a trade-off between speed and controllability, and that its excitatory connectivity may be configured in a way that optimizes this trade-off.

Having established the roles played by single-cell and connectivity properties of different cell-types in the eight-population model, we fixed these parameters and analyzed the behavior of the model over the range of possible tonic drives to fast and slow populations (Supplemental Figure S2). Similar to the two-population model, the eight-population with coupled fast and slow speed modules model exhibited head-to-tail propagation with constant phase lag (Supplemental Figure S2G), left-right alternation (Supplemental Figure S2F), and frequency-dependent recruitment of fast and slow populations (Supplemental Figure S2E). In addition to varying the frequency of oscillations, we also found that the overall amplitude of interneuron activity in the model could be varied by co-varying the drives to the fast and slow populations (Supplemental Figure S2C-D). This provides a potential mechanism to independently control frequency and amplitude of locomotion, although the manner in which the amplitude of interneuron activity relates to the amplitude of locomotion would depend on the assumptions made about how interneuron activity drives the

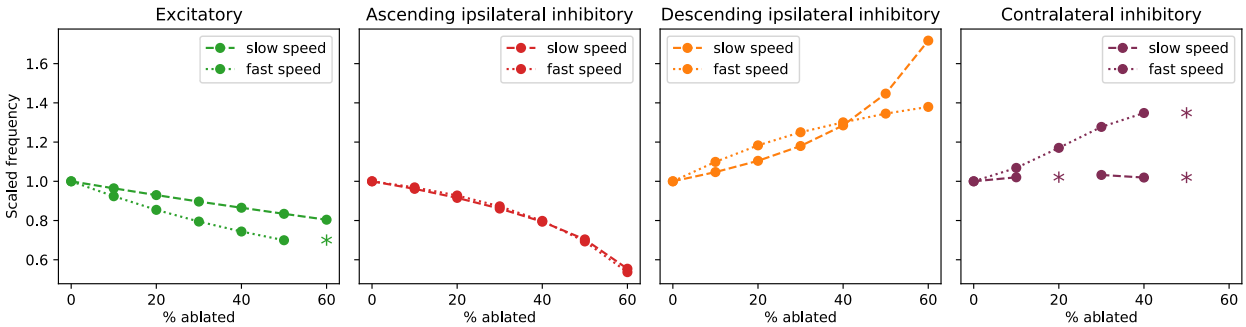

Figure 7: Ablating populations affects locomotion frequency and amplitude Dependence of locomotion frequency (normalized to its unperturbed value) on ablation of each of the four interneuron populations during slow speed oscillations (dashed lines; fast drive = 1.0, slow drive = 1.0; frequency = 9.3 Hz) and fast speed oscillations (dotted lines; fast drive = 2.0, slow drive = 0.5; frequency = 34.0 Hz). Asterisks mark points where the model failed to produce a coherent oscillation (see Methods).

activity of motor neurons, which we have not included in our models.

We next investigated the effects of perturbing the model by partially ablating (*i.e.* attenuating the outgoing activity of) each interneuron population (Figure 7). At all locomotion speeds, we found that ablating excitatory units decreased locomotion frequency. This is in agreement with experiments in zebrafish, where ablation of excitatory V2a interneurons had the same effect [41]. Further, we found that ablating inhibitory units with ascending ipsilateral projections decreased locomotor frequency, while ablating inhibitory units with descending projections increased locomotor frequency across all locomotion speeds. This is also in agreement with experiments in zebrafish, where ablation of inhibitory V1 interneurons slowed swimming [42], while ablation of V2b interneurons led to faster swimming [33, 21]. Finally, we found that ablating the contralaterally projecting inhibitory units led to a modest increase in frequency, but that coordinated locomotion was lost when the degree of ablation became too great. The impact on frequency was most obvious at fast speeds, with a more modest impact at slow speeds. This is consistent with recent experiments in zebrafish, which found the impact of attenuating contralateral inhibitory projections from dI6 neurons on coordination was most obvious at fast speeds [13]. Similar results were found in *Xenopus*, where silencing contralaterally projecting inhibitory interneurons can eliminate rhythm generation [15] or leads to an increase in swim frequency [43]. Together, these results show that, where comparisons with experimental data are possible, perturbations to our model lead to effects on locomotion frequency that generally agree with experimental observations. This agreement provides support for the possibility that the basic mechanisms underlying variable-frequency locomotion in our model—namely cell-type-specific connectivity patterns and speed-module recruitment—may also be at play in the spinal locomotor network.

Robustness in a biophysical model

One potential pitfall with the "rate models" considered above is that the oscillatory behavior seen in these models might be overwhelmed by the inherent stochasticity of a biophysical setting. To test the robustness of our connectivity-based mechanisms for rhythmogenesis and frequency control, we built a spiking-neuron version of each model.

The spiking models were generated from the rate models by replacing each unit in the rate model with n leaky-integrate-and-fire (LIF) neurons. A rough estimate suggests that the locomotor circuit is made up of 50-100 neurons of each cell type per segment[13, 33, 34, 44]. In accordance with this estimate, most of our simulations use $n = 80$, though versions with smaller n also performed well (Supplemental Figure S4). Connectivity between neurons in the spiking model was determined by including a random fraction p of all possible connections between groups of neurons corresponding to connected units in the rate model. The strength of these connections was determined by the strength of the corresponding connection in the rate model (for details see Methods).

In addition to the stochasticity introduced via the randomized connectivity, we introduced stochasticity in the spiking model by replacing of the tonic input drive of the rate model with EI-balanced Poisson input. This input was independently sampled for each neuron, with a uniform rate for each speed population. In the rate model, a given tonic drive represented the firing rate that an isolated unit would maintain without recurrent connections. To similarly control the input to the spiking model, the rates of the EI-balanced Poisson inputs were chosen to produce a target firing rate in an isolated LIF neuron. Since frequency control depended primarily on the ratio of the fast and slow tonic drives, and the target firing needed to be high enough to ensure spikes would occur reliably within the maxima of the oscillations, we chose our target rates to be 100 Hz times the equivalent tonic drive.

The spiking version of the single-population model demonstrated left-right alternation and head-to-tail propagation (Figure 8A). As with the rate model, the frequency of firing rate oscillations in this model did not depend on the input drive but did depend on the membrane time constant (Supplemental Figure S4C). We found that coherent oscillatory behavior survived at $n = 80$ even when the connectivity fraction p was reduced down to 0.05 (i.e. only 5% of connections are made), but that oscillations broke down for smaller values of p (Supplemental Figure S4A). At $n = 10$, we found that the cutoff for stable oscillations was $p = 0.6$ (Supplemental Figure S4B).

We next simulated the spiking model with fast and slow populations, the counterpart to our 2-population rate model (Figure 8B). Choosing the membrane time constants to be the same as the rate model (i.e. 1 ms for the fast population and 10 ms for the slow population) led to issues with controllability. In particular, it led to a breakdown of coherent oscillations at intermediate driving. Referring to our results with the single-population model, we hypothesized that this was caused by the large discrepancy between the natural frequencies of the fast and slow populations. Choosing the membrane time constants to be 2 ms for the fast population and 10 ms for the slow population, we recovered frequency control. As in the rate model, this frequency control was independent of amplitude control (Figure 8C). While the connectivity fraction p did not not affect controllability

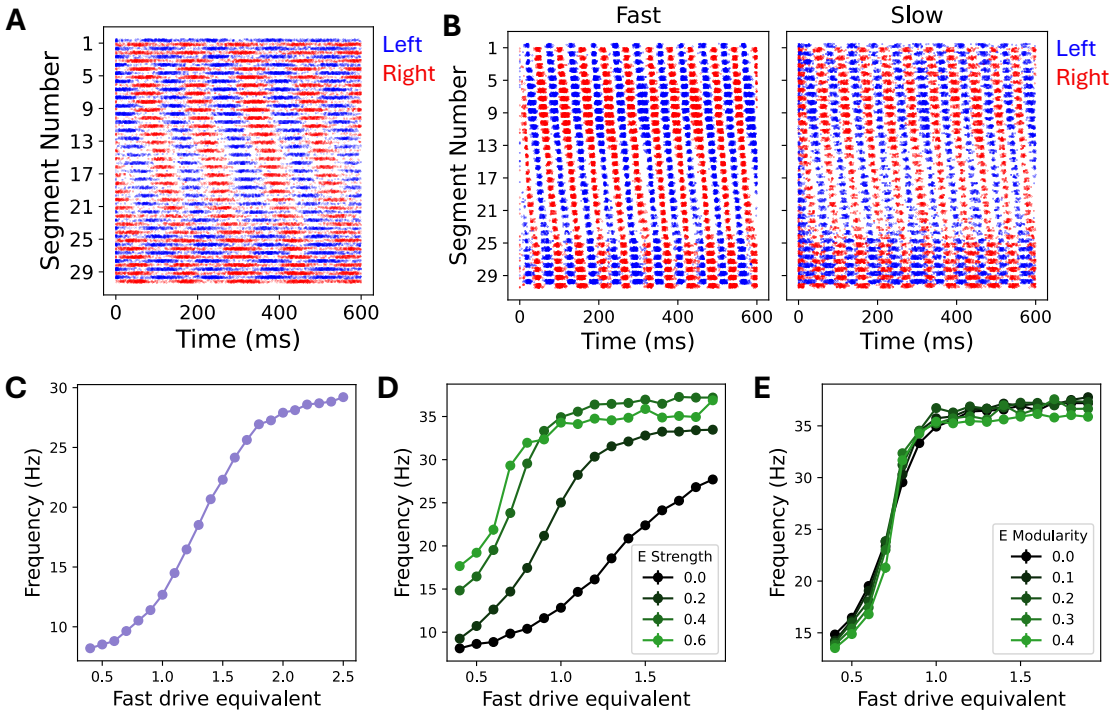

Figure 8: A spiking network model confirms that network-based mechanisms for rhythmogenesis and frequency control are robust in stochastic settings. **A**: A raster plot from the single-population spiking model. The blue (red) dots show spikes from neurons on the left (right) side of the spinal cord. **B**: A raster plot from the 2-population spiking model, with spikes from the fast (slow) population shown in the left (right) panel. **C**: Dependence of the frequency in the 2-population spiking model on the driving rate. Given a fast drive equivalent, f, the EI-balanced Poisson inputs have rates chosen to produce $f \times 100$ Hz in an isolated fast neuron and $1/f \times 100$ Hz in an isolated slow neuron. **D**: Dependence of the frequency in the 8-population spiking model on the strength of excitatory connections relative to the strength of inhibitory connections. The simulations shown here use 0 modularity for all populations. **E**: Dependence of the firing rate oscillations in the 8-population spiking model on the modularity of the excitatory connections. The simulation uses an excitatory connection strength of 0.4 and 0 modularity for the inhibitory connections. All spiking model simulations shown here use $n = 80$ LIF neurons for each unit of the corresponding rate model and connectivity fraction $p = 0.1$.

in this model, it did change the maximum frequency of the network (Supplemental Figure S4D).

Extending our spiking model to the full 8 populations of our final rate model (*i.e.*, dividing the inhibitory population into 3 separate populations and including an excitatory population), we again observed stable oscillations with left-right alternation, head-to-tail propagation, and controllable frequency with constant phase lag. As with the rate model, we varied the strength and modularity of the excitatory connections (Figure 8D,E). As in the rate model, increasing in excitatory connection strength increased the maximum frequency (Figure 8D). Rather than a loss of controllability at intermediate frequencies as in the rate model, however, the range of possible frequencies was instead reduced via an increase in the lowest frequency achieved by the network, suggesting that the fast population dominates the dynamics in the spiking network. Moreover, in contrast to the rate model, there was no change in maximum frequency upon increasing the modularity among excitatory units (Figure 8E), suggesting a possible saturation effect whereby the fast population already dominates the large-frequency dynamics of the network even at low degrees of modularity. Although this spiking network model responded somewhat differently than the rate models to certain parameter changes, the fact that rhythmogenesis and frequency control emerge from this model without fine tuning supports the conclusion that network-level interactions driven by cell-type-specific connectivity patterns are sufficient for producing locomotor behavior in a more biophysically detailed model.

Discussion

In this study, we began by postulating that cell-type-specific connectivity alone could be sufficient for producing the main phenomenological features of the spinal locomotor circuit, without requiring dynamical single-cell properties. We found that coordinated locomotion could be achieved in an inhibition-dominated network in which connectivity is determined by desired phase relationships and variable-speed control is implemented by recruitment of frequency-selective populations. Further, while structured excitatory connections were not necessary for producing coordinated locomotion or frequency control, they were useful for increasing peak locomotor frequency, albeit at the cost of losing some control at intermediate frequencies. Together, this family of models shows that network-level interactions are sufficient to generate coordinated, variable-speed locomotion. It further provides new interpretations of intersegmental excitatory and inhibitory connectivity, as well as the basic, recruitment-based mechanism of speed control.

A main conclusion of our models is the importance of intersegmental, inhibition-dominated connections for achieving coordinated locomotion, where patterns of ipsilateral and contralateral inhibition are established by desired phase relationships. Similarly, a very recent network-level model based on the mouse locomotor circuit has proposed that these are key features for obtaining coordinated locomotion in that context as well [45]. In addition, a recent study found that patterning recurrent neural network on the locomotor circuitry of *C. Elegans* produced a system that required fewer parameters and less training data than general multi-layer perceptron models for controlling a swimming agent [46]. The congruence of these results—all of which rely on emergent dynamics

driven by cell-type-specific connectivity patterns to generate rhythm, without requiring complex intracellular dynamics—suggests that network-level interactions are likely key drivers of locomotor dynamics across species and fit cross-species observations of spinal interneuron diversity. However, while these results suggest that intrinsic cellular mechanisms are not necessary to generate coordinated locomotor rhythms, they are certainly sufficient in certain circumstances, as demonstrated by previous lesion and pharmacological studies [9].

Another conclusion of our models is that both projection strength and modularity among fast and slow excitatory units increase the maximum possible frequency, but at the cost of losing some control at intermediate frequencies. Recent studies in zebrafish suggest the possiblity that the spinal circuit may overcome this limitation by having multiple subtypes of excitatory interneurons with different degrees of modularity. Specifically, V2a neurons with descending-only axons exhibit a greater degree of speed-dependent recruitment (suggesting a higher level of modularity), while those with bifurcating axons exhibit less [13]. Moreover, V2a neurons with bifurcating axons fire more reliably, compared to more sparsely firing descending-only V2a neurons, and they form stronger connections to motor neurons [40, 13], consistent with a hierarchical organization distinguishing interneuron rhythmogenesis from motor neuron recruitment. Including motor neurons and these distinct subtypes into a model and testing their effects will be an interesting direction for future work.

Given that the models that we have presented favor simplicity over realism, attempting to capture as much phenomenology as possible with a minimal number of tunable parameters, they are undoubtedly missing features that may be important for describing more-nuanced functional aspects of locomotion in aquatic vertebrates. For instance, we did not include in our model variations in intersegmental projection distances for dI6 and V0d neurons related to speed [47], nor did we include excitatory commissural interneuron classes, including V0v [48] and V3 interneurons [49]. Moreover, other recent models of the locomotor circuit in zebrafish have highlighted the importance of electrical synapses for rapidly initiating swim bouts and characterizing early stages of development [50, 51, 52]. Including these components would be a worthwhile extension of the models presented here. Finally, investigating the ways in which the circuit-level rhythm genesis of our model might work together with and complement mechanisms based on intracellular dynamics, as assumed in classical models, will be an important direction for future work.

A somewhat unique aspect of our approach has been to develop a *hierarchy of models* to describe the same neural circuit at varying levels of detail. (See also the related approach in Ref. [51], which developed a series of models describing the same circuit at different stages in development.) Having such a family of models that fit within the same modeling framework enabled us to (i) use the higher-level models to better motivate the choices made in our lower-level models and (ii) draw connections between models at different levels to gain additional insight into the functional roles of particular populations. Following this approach, we thus obtained greater insight into the neural mechanisms underlying behavior than would be possible from any one model individually. We expect that this general approach could be useful more broadly for characterizing neural circuits and their relation to behavior.

Acknowledgments

We are grateful for discussions with Martha Bagnall. This work was supported by the National Institutes of Health BRAIN Initiative (U01-NS136458).

References

[1] Thomas Graham Brown and Charles Scott Sherrington. The intrinsic factors in the act of progression in the mammal. *Proceedings of the Royal Society of London. Series B, Containing Papers of a Biological Character*, 84(572):308–319, 1911.

[2] S Grillner and P Wallén. Central pattern generators for locomotion, with special reference to vertebrates. *Annual review of neuroscience*, 8(1):233–261, 1985.

[3] Agnes Bonnot, Patrick J Whelan, George Z Mentis, and Michael J O'Donovan. Spatiotemporal pattern of motoneuron activation in the rostral lumbar and the sacral segments during locomotor-like activity in the neonatal mouse spinal cord. *The Journal of neuroscience*, 22(3):203–RC203, 2002.

[4] Sergiy Yakovenko, Vivian Mushahwar, Veronique VanderHorst, Gert Holstege, and Arthur Prochazka. Spatiotemporal activation of lumbosacral motoneurons in the locomotor step cycle. *Journal of neurophysiology*, 87(3):1542–1553, 2002.

[5] Jean-René Cazalets. Metachronal propagation of motoneurone burst activation in isolated spinal cord of newborn rat. *The Journal of physiology*, 568(2):583–597, 2005.

[6] Y. P. Ivanenko, R. E. Poppele, and F. Lacquaniti. Spinal cord maps of spatiotemporal alpha-motoneuron activation in humans walking at different speeds. *Journal of Neurophysiology*, 95(2):602–618, 2006. PMID: 16282202.

[7] Carlos A. Cuellar, Jesus A. Tapia, Victoria Juárez, Jorge Quevedo, Pablo Linares, Lourdes Martínez, and Elias Manjarrez. Propagation of sinusoidal electrical waves along the spinal cord during a fictive motor task. *Journal of Neuroscience*, 29(3):798–810, 2009.

[8] Philippe Saltiel, Andrea d'Avella, Kuno Wyler-Duda, and Emilio Bizzi. Synergy temporal sequences and topography in the spinal cord: evidence for a traveling wave in frog locomotion. *Brain Structure and Function*, 221(8):3869–3890, 2016.

[9] Sten Grillner and Alexander Kozlov. The cpgs for limbed locomotion–facts and fiction. *International journal of molecular sciences*, 22(11):5882–, 2021.

[10] Vladimir Rancic and Simon Gosgnach. Recent insights into the rhythmogenic core of the locomotor cpg. *International Journal of Molecular Sciences*, 22(3):1394, 2021.

[11] Sten Grillner and Abdeljabbar El Manira. The intrinsic operation of the networks that make us locomote. *Current Opinion in Neurobiology*, 31:244–249, 2015.

[12] Jianren Song, Irene Pallucchi, Jessica Ausborn, Konstantinos Ampatzis, Maria Bertuzzi, Pierre Fontanel, Laurence D. Picton, and Abdeljabbar El Manira. Multiple rhythm-generating circuits act in tandem with pacemaker properties to control the start and speed of locomotion. *Neuron*, 105(6):1048–1061.e4, 2020.

[13] Moneeza A Agha, Sandeep Kishore, and David L McLean. Cell-type-specific origins of locomotor rhythmicity at different speeds in larval zebrafish. *eLife*, July 2024.

[14] James T Buchanan and DR McPherson. The neuronal network for locomotion in the lamprey spinal cord: evidence for the involvement of commissural interneurons. *Journal of Physiology-Paris*, 89(4-6):221–233, 1995.

[15] Peter R Moult, Glen A Cottrell, and Wen-Chang Li. Fast silencing reveals a lost role for reciprocal inhibition in locomotion. *Neuron*, 77(1):129–140, 2013.

[16] Laurence D Picton, E Rebecka Björnfors, Pierre Fontanel, Irene Pallucchi, Maria Bertuzzi, and Abdeljabbar El Manira. Developmental switch in the function of inhibitory commissural v0d interneurons in zebrafish. *Current Biology*, 32(16):3515–3528, 2022.

[17] Henrik Lindén, Peter C. Petersen, Mikkel Vestergaard, and Rune W. Berg. Movement is governed by rotational neural dynamics in spinal motor networks. *Nature*, 610(7932):526–531, Oct 2022.

[18] David L McLean and Joseph R Fetcho. Movement, technology and discovery in the zebrafish. *Current opinion in neurobiology*, 21(1):110–115, 2011.

[19] Mohini Sengupta and Martha W Bagnall. Spinal interneurons: Diversity and connectivity in motor control. *Annu Rev Neurosci*, 46:79–99, February 2023.

[20] Evdokia Menelaou, Cassandra VanDunk, and David L. McLean. Differences in the morphology of spinal v2a neurons reflect their recruitment order during swimming in larval zebrafish. *Journal of Comparative Neurology*, 522(6):1232–1248, 2014.

[21] Mohini Sengupta and Martha W. Bagnall. V2b neurons act via multiple targets in spinal motor networks. *bioRxiv*, 2022.

[22] William A Alaynick, Thomas M Jessell, and Samuel L Pfaff. Snapshot: spinal cord development. *Cell*, 146(1):178–178, 2011.

[23] Martyn Goulding. Circuits controlling vertebrate locomotion: moving in a new direction. *Nature Reviews Neuroscience*, 10(7):507–518, Jul 2009.

[24] Avis H. Cohen, G. Bard Ermentrout, Tim Kiemel, Nancy Kopell, Karen A. Sigvardt, and Thelma L. Williams. Modelling of intersegmental coordination in the lamprey central pattern generator for locomotion. *Trends in Neurosciences*, 15(11):434–438, 1992.

[25] KAREN A. SIGVARDT and WILLIAM L. MILLER. Analysis and modeling of the locomotor central pattern generator as a network of coupled oscillators. *Annals of the New York Academy of Sciences*, 860(1):250–265, 1998.

[26] Sten Grillner, Alexander Kozlov, Paolo Dario, Cesare Stefanini, Arianna Menciassi, Anders Lansner, and Jeanette Hellgren Kotaleski. Modeling a vertebrate motor system: pattern generation, steering and control of body orientation. In Paul Cisek, Trevor Drew, and John F. Kalaska, editors, *Computational Neuroscience: Theoretical Insights into Brain Function*, volume 165 of *Progress in Brain Research*, pages 221–234. Elsevier, 2007.

[27] Jessica Ausborn, Natalia A. Shevtsova, and Simon M. Danner. Computational modeling of spinal locomotor circuitry in the age of molecular genetics. *International Journal of Molecular Sciences*, 22(13), 2021.

[28] K Zhang. Representation of spatial orientation by the intrinsic dynamics of the head-direction cell ensemble: a theory. *Journal of Neuroscience*, 16(6):2112–2126, 1996.

[29] Alexei Samsonovich and Bruce L McNaughton. Path integration and cognitive mapping in a continuous attractor neural network model. *Journal of Neuroscience*, 17(15):5900–5920, 1997.

[30] James M Murray and G Sean Escola. Learning multiple variable-speed sequences in striatum via cortical tutoring. *eLife*, 6:e26084, may 2017.

[31] Carina Curto and Katherine Morrison. Graph rules for recurrent neural network dynamics. *Not. Am. Math. Soc.*, 70(4):536–551, 2023.

[32] Shin-ichi Higashijima, Mark A Masino, Gail Mandel, and Joseph R Fetcho. Engrailed-1 expression marks a primitive class of inhibitory spinal interneuron. *Journal of Neuroscience*, 24(25):5827–5839, 2004.

[33] Rebecca A Callahan, Richard Roberts, Mohini Sengupta, Yukiko Kimura, Shin-ichi Higashijima, and Martha W Bagnall. Spinal v2b neurons reveal a role for ipsilateral inhibition in speed control. *Elife*, 8:e47837, 2019.

[34] Mohini Sengupta, Vamsi Daliparthi, Yann Roussel, Tuan V. Bui, and Martha W. Bagnall. Spinal v1 neurons inhibit motor targets locally and sensory targets distally. *Current Biology*, 31(17):3820–3833.e4, 2021.

[35] David L. McLean, Mark A. Masino, Ingrid Y. Y. Koh, W. Brent Lindquist, and Joseph R. Fetcho. Continuous shifts in the active set of spinal interneurons during changes in locomotor speed. *Nature Neuroscience*, 11(12):1419–1429, Dec 2008.

[36] Vladimir Rancic, Klaus Ballanyi, and Simon Gosgnach. Mapping the dynamic recruitment of spinal neurons during fictive locomotion. *Journal of Neuroscience*, 40(50):9692–9700, 2020.

[37] Evdokia Menelaou, Sandeep Kishore, and David L McLean. Mixed synapses reconcile violations of the size principle in zebrafish spinal cord. *eLife*, 11:e64063, sep 2022.

[38] Avinash Pujala and Minoru Koyama. Chronology-based architecture of descending circuits that underlie the development of locomotor repertoire after birth. *Elife*, 8:e42135, 2019.

[39] Frances K Skinner and Brian Mulloney. Intersegmental coordination in invertebrates and vertebrates. *Current opinion in neurobiology*, 8(6):725–732, 1998.

[40] Evdokia Menelaou and David L. McLean. Hierarchical control of locomotion by distinct types of spinal v2a interneurons in zebrafish. *Nature Communications*, 10(1):4197, Sep 2019.

[41] Emma Eklöf-Ljunggren, Sabine Haupt, Jessica Ausborn, Ivar Dehnisch, Per Uhlén, Shin-ichi Higashijima, and Abdeljabbar El Manira. Origin of excitation underlying locomotion in the spinal circuit of zebrafish. *Proceedings of the National Academy of Sciences*, 109(14):5511–5516, 2012.

[42] Yukiko Kimura and Shin-ichi Higashijima. Regulation of locomotor speed and selection of active sets of neurons by v1 neurons. *Nature communications*, 10(1):2268, 2019.

[43] Nicholas Dale. Experimentally derived model for the locomotor pattern generator in the xenopus embryo. *The Journal of Physiology*, 489(2):489–510, 1995.

[44] Sandeep Kishore, Eli B. Cadoff, Moneeza A. Agha, and David L. McLean. Orderly compartmental mapping of premotor inhibition in the developing zebrafish spinal cord. *Science*, 370(6515):431–436, 2020.

[45] Salif Komi, August Winther, Grace A. Houser, Roar Jakob Sørensen, Silas Dalum Larsen, Madelaine C. Adamssom Bonfils, Guanghui Li, and Rune W. Berg. Spatial and network principles behind neural generation of locomotion. *bioRxiv*, 2024.

[46] Nikhil Bhattasali, Anthony M Zador, and Tatiana Engel. Neural circuit architectural priors for embodied control. In S. Koyejo, S. Mohamed, A. Agarwal, D. Belgrave, K. Cho, and A. Oh, editors, *Advances in Neural Information Processing Systems*, volume 35, pages 12744–12759. Curran Associates, Inc., 2022.

[47] Chie Satou, Takumi Sugioka, Yuto Uemura, Takashi Shimazaki, Pawel Zmarz, Yukiko Kimura, and Shin-ichi Higashijima. Functional diversity of glycinergic commissural inhibitory neurons in larval zebrafish. *Cell Reports*, 30(9):3036–3050, 2020.

[48] Kohei Kawano, Kagayaki Kato, Takumi Sugioka, Yukiko Kimura, Masashi Tanimoto, and Shin-ichi Higashijima. Long descending commissural v0v neurons ensure coordinated swimming movements along the body axis in larval zebrafish. *Scientific Reports*, 12(1):4348, 2022.

[49] Urs L Böhm, Yukiko Kimura, Takashi Kawashima, Misha B Ahrens, Shin-ichi Higashijima, Florian Engert, and Adam E Cohen. Voltage imaging identifies spinal circuits that modulate locomotor adaptation in zebrafish. *Neuron*, 110(7):1211–1222, 2022.

[50] Yann Roussel, Melissa Paradis, Stephanie F Gaudreau, Ben W Lindsey, and Tuan V Bui. Spatiotemporal transition in the role of synaptic inhibition to the tail beat rhythm of developing larval zebrafish. *Eneuro*, 7(1), 2020.

[51] Yann Roussel, Stephanie F Gaudreau, Emily R Kacer, Mohini Sengupta, and Tuan V Bui. Modeling spinal locomotor circuits for movements in developing zebrafish. *Elife*, 10:e67453, 2021.

[52] Lae Un Kim and Hermann Riecke. Intersegmental coordination of the central pattern generator via interleaved electrical and chemical synapses in zebrafish spinal cord. *Journal of Computational Neuroscience*, 51(1):129–147, 2023.

[53] Marcel Stimberg, Romain Brette, and Dan FM Goodman. Brian 2, an intuitive and efficient neural simulator. *eLife*, 8:e47314, August 2019.

[54] Wulfram Gerstner, Werner M. Kistler, Richard Naud, and Liam Paninski. *Neuronal Dynamics: From Single Neurons to Networks and Models of Cognition*. Cambridge University Press, USA, 2014.

Methods

Simulation details

The multi-segment model has 30 segments and 2 sides (left and right), for a total of 60 hemi-segments. Each hemi-segment contains one unit corresponding to each neuron type. In the 1-population model, there is only one inhibitory neuron type; in the 2-population model, there are both fast and slow types of inhibitory neurons; in the 8-population model there is a fast and slow type of each of excitatory, ascending ipsilateral inhibitory, descending ipsilateral inhibitory, and contralateral inhibitory neuron type.

The state of each unit is described by its firing rate as a function of time. The time course is calculated by Equation 1, where h_i is the activity of unit i, and $[\cdot]_+ = \text{ReLU}()$ is the rectified-linear function. The membrane time constants are set to 1ms (10ms) for the fast (slow) module, or 1ms in models with no speed modules.

The numerical simulation was performed using Euler's method with timestep equal to 0.1ms. For all simulations considered in this work, the simulation was run for 600 ms (or 6000 timesteps). The firing rate of each unit is set to a small random rate sampled uniformly from [0, 0.01] at $t = 0$ in order to break symmetry.

For the 1-population model there were no synaptic time delays included. In the 2- and 8-population models, synaptic time delays are equal to:

$$\tau_{delay} * (1 + \Delta_S) \tag{4}$$

Where τ_{delay} is the base delay amount, and Δ_S is the distance (measured in number of segments) between the pair of units which the connection is between (Δ_S=0 when the units are in the same segment). For the 2- and 8-population models, τ_{delay} is set to 0.2 ms for the fast population and 0.5 ms for the slow population, matching roughly the experimentally measured axonal conduction velocities detailed in Ref. [40]. Note that the synaptic time delays are determined by the identity of the source unit, not the target unit.

Units in the model are driven by a constant tonic input. This drive is varied separately for the fast and slow populations. In addition, each unit receives recurrent input from the other units according to the interneuron connectivity W_{ij}, which represents the strength of the connection from unit j to i. The connectivity matrices, W_{ij}, are shown in Figures 1B, 2B, and 4B.

The base value of inhibitory projections is set to -0.5. The base strength for the excitatory connections is set to $0.5f_E$, where the multiplicative factor f_E takes a value between 0 and 1 and determines the strength of excitation relative to inhibition. Except when this parameter is explicitly varied (see Figure 6), we set $f_E = 0.4$.

In the 2-population and 8-population models, we introduce the speed mixing factor, f_{sm}. The connection strengths for all fast-to-fast and slow-to-slow connections were multiplied by $(1 - f_{sm})$, whereas all fast-to-slow and slow-to-fast connection strengths were multiplied by f_{sm}. This generates a modularity of $m = 1 - 2f_{sm}$. In the case of the 8-population model, we can apply a global speed mixing factor f_{sm} or a separate speed mixing factor for the excitatory population $f_{sm,E}$ and

for the inhibitory population $f_{sm,I}$. The results of varying these parameters are shown in Figure 6.

Ablation was introduced as an overall factor, f_A, that multiplied the connection strengths of all connections sourced from the ablated population. This then implies that

$$\% \text{ ablation} = (1 - f_A) \times 100\% \,. \tag{5}$$

Analysis methods

The output of the simulation is a collection of time series giving the firing rate of each unit as a function of time. By inspection, it was clear that the time series settled into a sensible oscillation after an initialization period. To ensure the observations corresponded to the stable oscillatory mode, all analysis was performed on the times series from t=100ms to t=600ms (i.e. we cut out the first 100ms).

For each unit's firing rate time series, $r(t)$, the amplitude is defined as the difference between the maximum and minimum values of the time series. That is

$$A = \max_t r(t) - \min_t r(t) \,. \tag{6}$$

The amplitude of the simulation is then defined as the mean amplitude across all units (or, if amplitude is reported for a particular population, across all units within that population). Errors are given by the standard deviation in amplitude across all units.

To extract the frequency of the time series $r(t)$, we calculated the period of each time series. To find the period, we considered the autocorrelation spectrum defined by:

$$C(k) = \sum_t r(t) r(t-k) \tag{7}$$

Here $r(t) = 0$ whenever t is outside the domain $t \in [100\text{ms}, 600\text{ms}]$. In all cases the maximum autocorrelation occurs at $k = 0$. In cases with a single dominant frequency as k increases away from zero, the autocorrelation drops to global minimum (which we define as $k = k_{\min}$) then rises to a local maximum at a value of k equal to the period (see Figure S3). This is then followed by a series of local minima and maxima of lesser size. Crucially, this local maximum can be isolated as the global maximum if we only consider $k > k_{\min}$. Hence, we define the period of $r(t)$ by

$$T = \text{argmax}_{k > k_{\min}} C(k), \tag{8}$$

and we define the frequency of $r(t)$ by $f = 1/T$. From there frequencies of the different unit types were averaged within each hemi-segment weighted by the amplitude. This amplitude-averaged frequency was then used to compute an unweighted mean frequency and standard deviation across all hemi-segments.

We calculate the phase ϕ of $r(t)$ as

$$\phi = \frac{1}{2\pi} \arg\left(\tilde{r}(\nu)\right) \tag{9}$$

Where $\arg(z)$ gives the argument (or phase) of the complex number z and $\tilde{r}(\nu)$ is the Fourier coefficient of r at the measured frequency, ν. Notice that we have normalized our phases to be in the range $(-1/2, 1/2]$ instead of $(-\pi, \pi]$. The phase difference $\Delta\phi_{ij}$ between phases ϕ_i and ϕ_j is calculated with

$$\Delta\phi_{ij} = \frac{1}{2\pi}\arg\left(e^{2\pi i(\phi_i - \phi_j)}\right) , \tag{10}$$

to avoid erroneously large phase differences for phases near $-\frac{1}{2}$ and $\frac{1}{2}$. Each phase difference at each location is averaged via a standard amplitude-weighted mean. A circular mean and circular standard deviation are used to then average the amplitude averaged phase differences across all hemi-segments.

Failures of coherent oscillation

Two issues arise that can prevent the extraction of a single well-defined frequency from a completed simulation: (i) There are multiple dominant frequencies in the time series for some units, or (ii) the frequencies do not agree between the fast and slow populations.

In the case of having multiple dominant frequencies, the autocorrelation spectrum no longer follows the easily interpretable shape described above. Rather, the time series and autocorrelation appear like the example in Figure S3E and S3F. A key observation is that the global minimum coincides with the first local minimum only in cases with a single dominant frequency. Therefore, to systematically find those time series with multiple dominant frequencies, we compare the frequency found using the *global* minimum as $k_{\min}$ with the frequency found using the first *local* minimum as $k_{\min}$.

In some cases (especially at high modularity), a well-defined frequency occurs within the fast population that differs significantly from a well-defined frequency within the slow population. This also demonstrates a failure for the system to oscillate coherently.

To systematically determine whether a simulation resulted in a well-defined frequency, we compare four frequency values:

1. The mean over the fast population of frequencies found using the global minimum
2. The mean over the slow population of frequencies found using the global minimum
3. The mean over the fast population of frequencies found using the first local minimum
4. The mean over the slow population of frequencies found using the first local minimum

Only if all values agree (to within a small tolerance) do we consider the frequency well-defined for the whole population.

Spiking model implementation

The spiking models were implemented using the Brian 2 software package [53].

Each spiking model is derived from the corresponding rate model by replacing each unit of the rate model with n current-based, leaky-integrate-and-fire (LIF) neurons. The spiking threshold was set to $V_t = 50$ mV and the reset potential was set to $V_r = 0$ mV. No refractory period was set for the LIF neurons.

For a connection in the rate model from unit i to unit j with non-vanishing weight W_{ij}, a fraction p of all possible connections from neurons in unit i to neurons in unit j are added to the spiking model. The strengths of these connections are given by

$$W_{\text{spiking}} = W_{ij}(V_t - V_r)\frac{10 \text{ ms}}{\tau_j}\frac{1}{n \cdot p}\,.$$

Our models employed delta function synapses, so that the currents due to recurrent connections were sums of weighted delta functions.

In place of a tonic external drive, each neuron in the spiking model receives independent EI-balanced Poisson noise. These external spikes are given a weight of $dv = \pm\frac{V_t - V_r}{10}$. The rate of the Poisson noise was chosen to promote a target firing rate in an isolated LIF neuron. Given a target rate ν_t, we find the corresponding Poisson rate ν_p by numerically solving the following equation (adapted from Equation 8.54 in [54]):

$$\frac{1}{\nu_t} = \tau\sqrt{\pi}\int_0^x \exp\left(u^2\right)\left(1 + \text{erf}(u)\right)du \tag{11}$$

with

$$x = \frac{V_t}{dv\sqrt{2\tau\nu_p}}\,. \tag{12}$$

Here erf is the error function. Target rates were chosen to be 100 Hz times the corresponding dimensionless tonic drive value.

All simulations were run with a 1 ns timestep for 600 ms total and the spikes of every neuron were recorded.

Detecting frequency in spiking network simulations

To extract the frequency of firing rate oscillations in the spiking models, we calculated the firing rate of each unit in 5 ms time bins by averaging the spike counts of all neurons in the unit. From these rates, an autocorrelation spectrum for each unit was calculated. When calculating the autocorrelation spectra, we discarded the initial 150 ms of the recording to avoid activity before the network settles into its stable oscillatory mode.

The rates and autocorrelation spectra for each unit are noisier than those measured in the rate model. This poses a possible challenge to our automatic frequency extraction pipeline by introducing or shifting the local minima and maxima of the autocorrelation spectra. To deal with this noise, we took an amplitude-weighted average of the autocorrelation spectrum to generate a global autocorrelation spectrum. To ensure that the shape of this spectrum is reasonable, frequencies are calculated from every peak and compared. The frequencies we report use the average of these frequency measurements. In addition, these frequencies were compared against the frequencies calculated from the fast and slow populations and using the local minium method described above.

Supplemental Figures

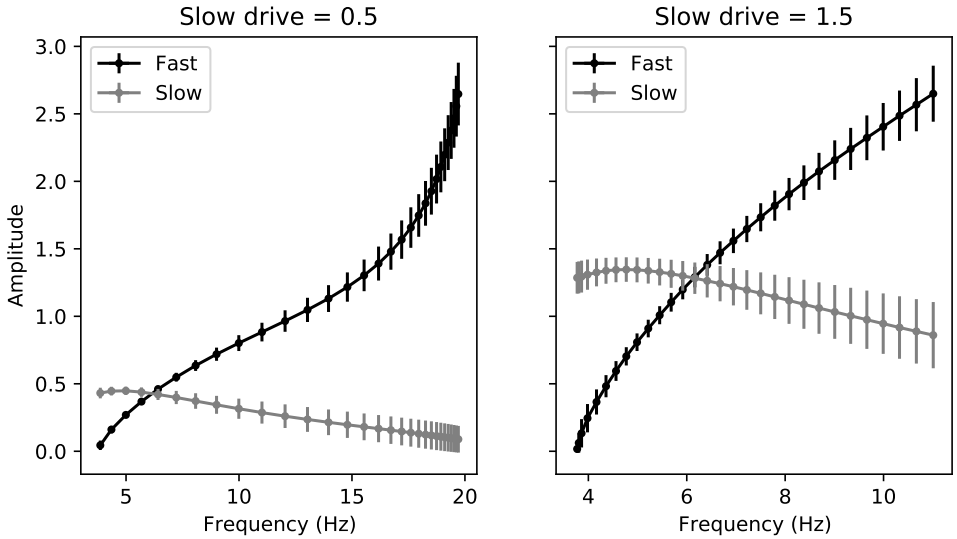

Supplemental Figure S1: Recruitment of fast module at high frequencies inhibits slow module. Data from Figure 3B plotted along paths with constant drive to the slow population (left: small drive; right: large drive) as drive to the fast population is varied.

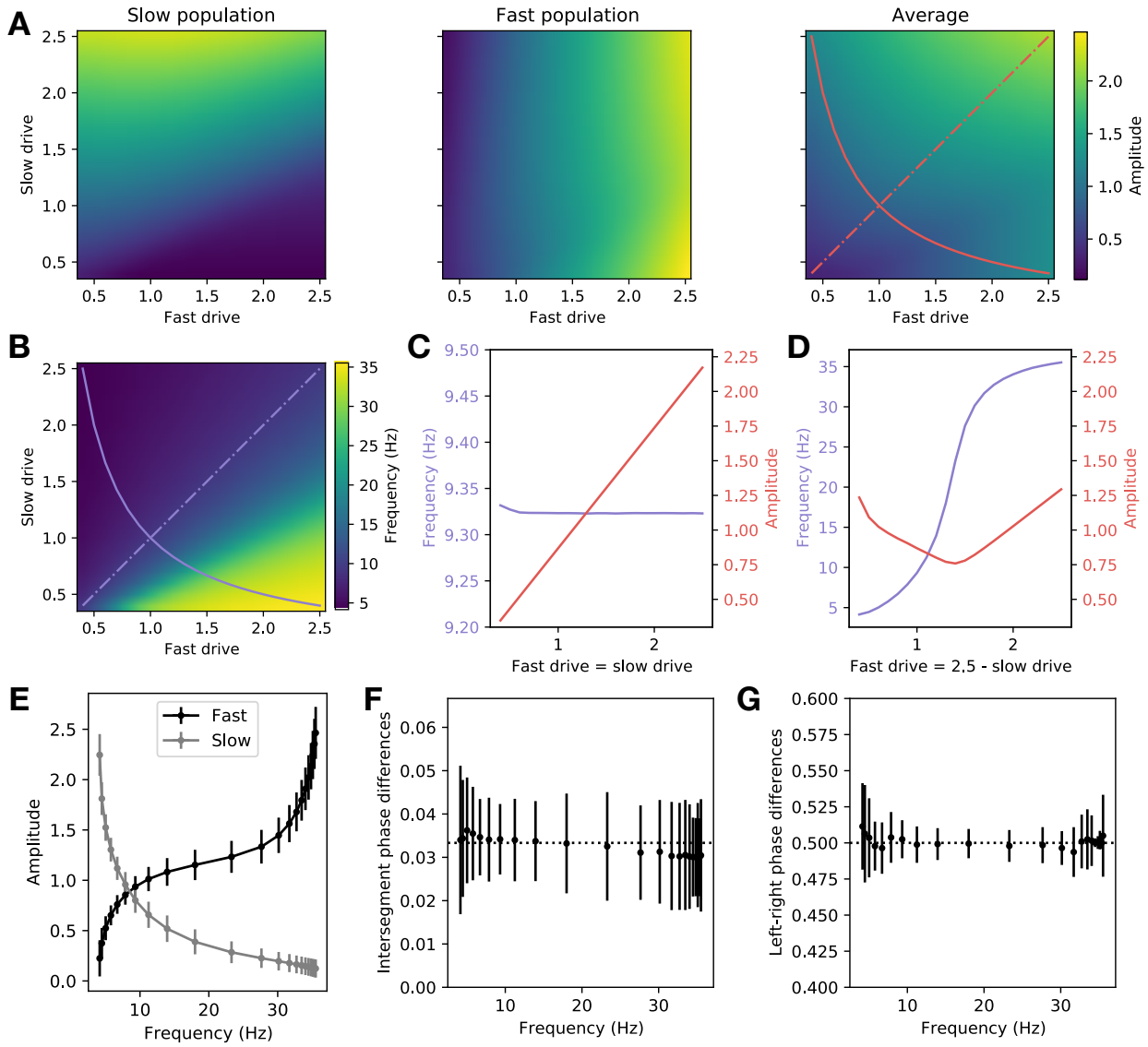

Supplemental Figure S2: Speed-module recruitment enables coordinated locomotion with frequency and amplitude control in an eight-population model **A**: Amplitude of the fast population (left), the slow population (center), and averaged over the fast and slow populations (right). **B**: Levels of tonic drive to the fast and slow populations determine locomotion frequency. **C**: Average amplitude and frequency along the path shown as a solid line in (A) and (B). **D**: Average amplitude and frequency along the path shown as a dash-dot line in (A) and (B). **E**: Frequency-dependent recruitment of fast and slow units as a function of locomotion frequency. **F**: Phase difference between units within each segment (dotted line corresponds to half of a period). **G**: Phase difference between pairs of units on the same side in adjacent segments (dotted line corresponds to $1/N$, where $N = 30$ is the number of segments). Error bars in all panels denote standard deviation across units.

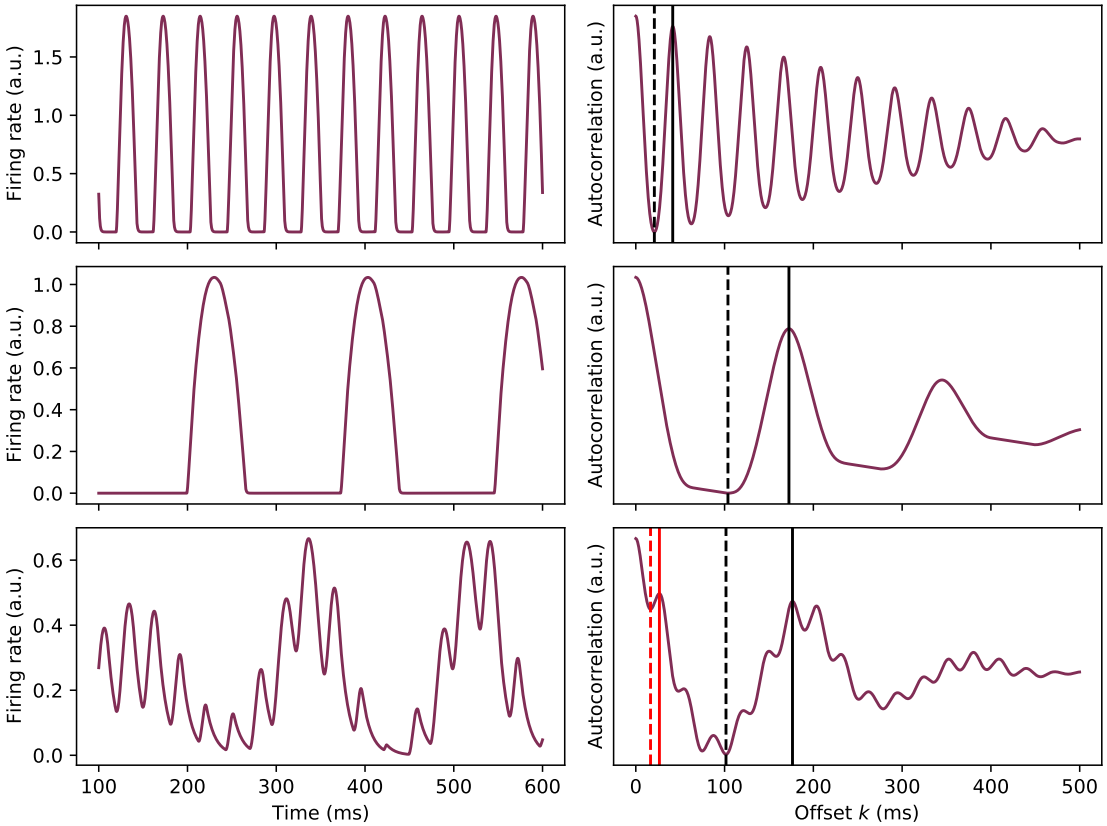

Supplemental Figure S3: Frequency determination from time series is performed through calculating the period from the autocorrelation spectrum. **A**: An example of a high-frequency rate time series from a single unit in the 8-population model. **B**: The autocorrelation spectrum corresponding to the time series in (A). The global minimum and resultant period are marked in dashed and solid lines, respectively. **C**: An example of a low frequency time series from a single unit in the 8-population model. **D**: The autocorrelation spectrum for the time series in (C). The global minimum and resultant period are marked in dashed and solid lines, respectively. **E**: An example time series without a single dominant frequency in the 8-population model. The failure was brought about by increasing the global strength of excitatory connections to 0.5 and the modularity to 0.4. **F**: The autocorrelation spectrum of the the time series in (E). The global minimum and resultant period are marked in dashed and solid black lines, respectively. The first local minimum and resultant period are marked in dashed and solid red lines, respectively.

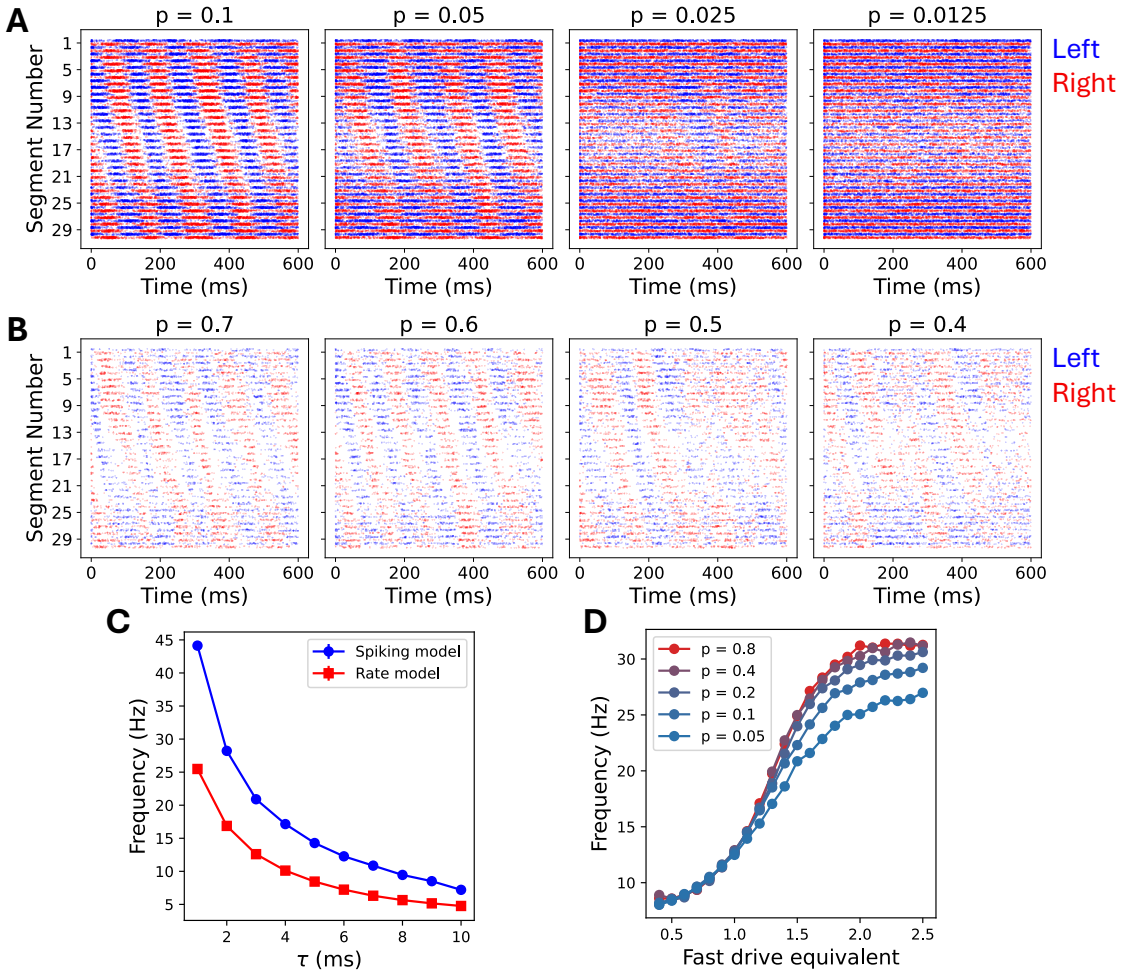

Supplemental Figure S4: Dependence of spiking model behavior on n, p, and τ. **A**: Raster plots for the $n = 80$ single-population spiking model at different values of p. The membrane time constant is $\tau = 10$ ms for these simulations. **B**: Raster plots for the $n = 10$ single-population spiking model at different values of p. The membrane time constant is $\tau = 10$ ms for these simulations. **C**: Dependence of the frequency of firing rate oscillations in the single-population model on the membrane time constant τ. The spiking model was simulated with $n = 80$ and $p = 0.1$. The rate model was simulated without synaptic time delays. **D**: Dependence of the frequency of firing rate oscillations in the 2-population model on p and the driving frequency. The simulations used $n = 80$.